$g\text{-}C_3N_4$ (2D)/ CdS (1D)/ rGO (2D) Dual-Interface Nano-Composite for Excellent and Stable Visible Light Photocatalytic Hydrogen Generation

Surendar Tonda [a,*], Santosh Kumar [b], Yogesh Gawli [c], Monika Bhardwaj [d], Satishchandra Ogale [d,*]

[a] Department of Chemistry and Centre for Energy Science, Indian Institute of Science Education and Research, Dr. Homi Bhabha Road, Pashan, Pune 411008, India

[b] European Bioenergy Research Institute, Aston University, Birmingham B4 7ET, UK

[c] Physical and Materials Chemistry Division, National Chemical Laboratory (CSIR-NCL), Pashan, Pune 411008, India

[d] Department of Physics and Centre for Energy Science, Indian Institute of Science Education and Research, Dr. Homi Bhabha Road, Pashan, Pune 411008, India

***Corresponding Authors:**

Satishchandra Ogale, E-mail: satishogale@iiserpune.ac.in; satishogale@gmail.com, Tel.: +91 20 2590 8292.

Surendar Tonda, E-mail: surendar.t86@gmail.com

Highlights

- g-C_3N_4/CdS/rGO (2D/1D/2D) dual-interface ternary composite system was developed.
- The ternary system showed excellent photocatalytic H_2 generation under visible-light.
- At an optimum CdS and rGO contents the ternary system exhibited QE of 11.1% (420 nm).
- The g-C_3N_4/CdS/rGO dual-interface system exhibited high photostability.
- Specific benefits of a dual-interface system over a single interface case are emphasized.

Graphical Abstract

g-C_3N_4 (2D)/ CdS (1D)/ rGO (2D) Dual-Interface Nano-Composite for Excellent and Stable Visible Light Photocatalytic Hydrogen Generation

Surendar Tonda, Santosh Kumar, Yogesh Gawli, Monika Bhardwaj, Satishchandra Ogale

A 2D/1D/2D dual-interface nano-heterostructure configuration in the form of CdS nanorods sandwiched between g-C_3N_4 and rGO sheets with intimate interfacial contact show excellent photocatalytic H_2 generation rate of ~4800 μmol h^{-1} g^{-1}, with quantum efficiency of 11.1% at 420 nm under visible-light irradiation.

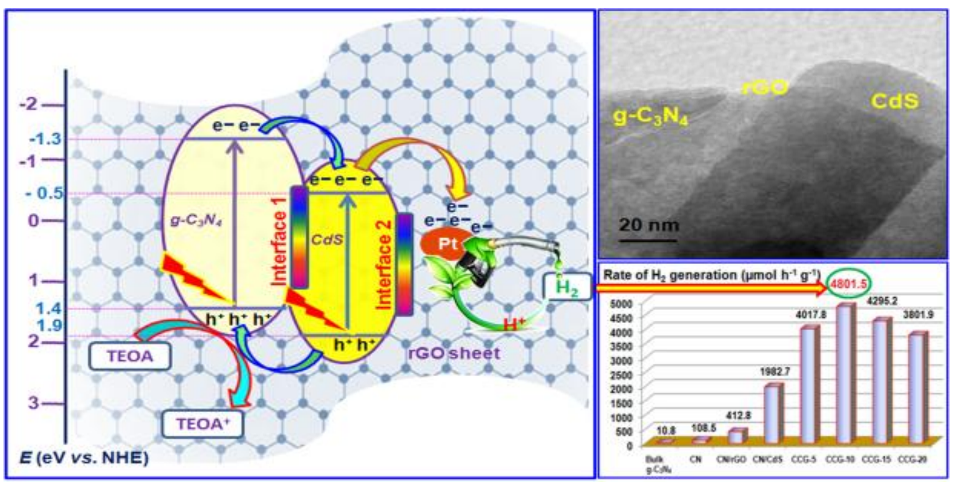

Abstract

A 2D/1D/2D dual-interface nano-composite configuration in the form of CdS nanorods sandwiched between g-C_3N_4 and rGO sheets with intimate interfacial contact is synthesized by a facile wet-chemical method and is shown to exhibit excellent photocatalytic H_2 generation under visible-light irradiation. In particular, the optimal g-C_3N_4/CdS/rGO dual-interface nano-composite shows H_2 production rate of ~4800 μmol h^{-1} g^{-1}, which is almost 44, 11 and 2.5 times higher than that shown by pure g-C_3N_4 nanosheets, and the g-C_3N_4/rGO and g-C_3N_4/CdS single interface heterostructures, respectively. It is shown that the synergic effects involving the band structure match and close interfacial contact, which can accelerate the separation and transfer of photoinduced charge carriers, and the enhanced visible-light absorption together contribute to the impressive photocatalytic performance and photostability of the g-C_3N_4/CdS/rGO ternary nano-composite system. Specific advantages of a dual-interface triple-composite system over a single interface case(s) are also brought out.

Key words: g-C_3N_4; H_2 generation; heterostructure; nano-composite, dual-interface; charge transfer

1. Introduction

The immense and ever growing demand for energy is driven by the growing world population and its constant demands for better living. In view of the serious environmental consequences of the current forms of energy that are being used for the development, finding ways and means to harvest, store and conserve renewable energy sources, has become the single most important and challenging research frontier for the modern world [1-4]. Photocatalytic hydrogen production by water splitting powered by renewable and sustainable solar energy is considered as the most promising and sustainable approach to meet the global energy demands and mitigating the associated environmental issues [5-8].

Since the discovery of hydrogen production through photoinduced water splitting on titanium dioxide (TiO_2) in 1972 [9], extensive efforts have been expended towards the development of photocatalysts for hydrogen production. Up to date, a large number of materials have been explored the said purpose including, sulfides (CdS [10], NiS [11], ZnS [12]), oxides (TiO_2 [13], ZnO [14]), mixed oxides with a perovskite structure ($SrTiO_3$ [15], $NaTaO_3$ [16]) etc. Nevertheless, some intrinsic drawbacks of these systems have still prevented their practical implementation for photocatalytic solar-hydrogen conversion. These include poor photostability, limited region of the effective visible-light photo response, short lifespan of photogenerated charge carriers, and complicated synthesis processes. To address these limitations, the designs and explorations of novel visible-light responsive photocatalysts with high efficiency are essential.

In recent years, graphitic carbon nitride (g-C_3N_4), particularly its two dimensional (2D) g-C_3N_4 nanosheet form, has attracted much attention in the H_2 production context due to its extraordinary properties including appropriate band gap (2.7 eV), large surface area, excellent chemical and thermal stabilities, non-toxicity, easy preparation, metal-free composition, and tunable electronic structure [17-20]. Indeed, owing to its fascinating properties, g-C_3N_4 has been regarded as a “sustainable” photocatalyst for solar energy conversion [21-25]. More importantly, this metal-free g-C_3N_4 is not only found to be a stable material, but also capable of achieving both half reactions of water splitting, implying that its suitable band edge potentials for both the water reduction and oxidation reactions [24]. This is indeed a fortunate and rare case. However, the photocatalytic efficiency of g-C_3N_4 is still far from the level required for practical applications because of the rapid recombination of photogenerated charge carriers therein and its low visible- light utilization efficiency. Thus, to improve its photocatalytic performance various interesting strategies have been exploited by different researchers, including morphology change, doping with metal or non-metal ions, loading co-catalysts and coupling with other semiconductor materials [26-32]. Among these, construction of nano-composites by combining different semiconductor materials with suitable band edge potentials is the most effective approach to promote the separation of photogenerated charge carriers [33].

Many researchers have explored g-C_3N_4–based coupled semiconductor photocatalysts, such as g-C_3N_4/TiO_2, g-C_3N_4/ZnO, g-C_3N_4/$SrTiO_3$, g-C_3N_4/WO_3, g-C_3N_4/CeO_2, g-C_3N_4/CdS, graphene/g-C_3N_4, and so on [34-40]. These interesting works have provided many insights into the key issues that need to be addressed by further work. For instance, Cao et al. [39] reported on the g-C_3N_4/CdS heterojunctions with well-matched band structures that could not only suppress the photocorrosion of CdS but also improve the visible-light absorption and charge separation of g-C_3N_4 to some extent. Another report on graphene/g-C_3N_4 composite by Xiang et al. [40] clearly demonstrated that graphene sheets act as electronic conductive channels to promote the separation of photogenerated electrons and holes, thereby improving the photocatalytic performance of g-C_3N_4. However, the overall activity of these materials is still below the desired range for their successful practical implementation, possibly due to the need to establish further synergy between the positive features of CdS (for example, its efficient light absorption) and graphene (for example, its electronic conductive channels to promote the separation of photogenerated electrons and holes). Moreover, inspired by the role of rGO as excellent support and fairly efficient electron transport material [41], and the role of CdS as a visible-light absorber and its excellent band structure match with g-C_3N_4, it is expected that the combination of g-C_3N_4

with CdS and rGO could render an efficient composite photocatalyst for H_2 production reaction. It is therefore highly desirable to construct such novel triple nano-composites that would not only enhance the separation of photogenerated electrons and holes, but also extend the optical absorption of g-C_3N_4, thereby allowing more efficient utilization of solar energy.

In the present study, a sandwich like dual-interface ternary nano-composite architecture composed of 2D g-C_3N_4 nanosheets, 1D CdS nanorods, and 2D rGO sheets were synthesized by a facile wet-chemical method. Such composites were thoroughly characterized by various analytical techniques. The photocatalytic activities of pure g-C_3N_4 nanosheets and g-C_3N_4/CdS/rGO dual-interface system were studied by monitoring the H_2 generation under visible-light irradiation. The role of rGO and significance of optimum CdS content for enhanced photocatalytic H_2 generation of the ternary nano-composite was carefully explored and the same is discussed in detailed. The reusability and photostability of the synthesized photocatalysts were also investigated through five successive experimental runs. A possible photocatalytic mechanism is also suggested based on the photoluminescence and photocurrent findings to demonstrate the extraordinary H_2 generation performance of g-C_3N_4/CdS/rGO triple nano-composite system under visible-light irradiation.

2. Experimental section

2.1 Materials

Melamine (Sigma-Aldrich, 99.0%), graphite powder (Sigma-Aldrich, 99.9%), cadmium acetate dihydrate (SDFCL, 99.9%), thioacetamide (Merck, AR grade), hydrogen peroxide (Merck, AR grade), hydrazine hydrate (Merck, AR grade), and triethanolamine (SRL, 98.0%) were used as received. All other reagents used in this work were of analytically pure grade and used without further purification. All aqueous solutions were prepared with deionized water.

2.2 Method

2.2.1 Synthesis of 2D g-C_3N_4 nanosheets. The bulk g-C_3N_4 was synthesized by one-step polymerization of melamine according to a procedure described in our previous paper [27]. In a typical process, the precursor melamine was thermally treated in a tube furnace at 550 °C for 2 h with a heating rate of 5 °C min^{-1} under N_2 atmosphere. The obtained yellow-colored bulk g-C_3N_4 was collected and ground into powder for further use.

The g-C_3N_4 nanosheets were obtained by liquid exfoliation of the as-synthesized bulk g-C_3N_4 in water. In detail, 0.1 g of bulk g-C_3N_4 powder was dispersed in 250 mL water and then ultrasonicated for about 15 h. The resulting suspension was centrifuged at about 5000 rpm to remove the residual unexfoliated g-C_3N_4 and then the supernatant suspension was heated at 100 °C. The obtained pale yellow colored g-C_3N_4 nanosheets are named as CN.

2.2.2 Synthesis of 1D CdS nanorods. The CdS nanorods were synthesized by the hydrothermal method. In a typical synthesis, a mixture of cadmium acetate dihydrate (0.5 g) and thioacetamide (0.25 g) was dissolved in ethylenediamine (50 mL) under vigorous stirring at room temperature for 30 min to obtain a uniform suspension. The obtained suspension was transferred into a 100 mL Teflon-lined stainless steel autoclave and heated to 200 °C for 3 h. After natural cooling to room temperature, the yellow precipitate was washed with water and ethanol through centrifugation several times, and dried in an oven at 60 °C for 12 h.

2.2.3 Synthesis of 2D reduced graphene oxide sheets. Graphene oxide (GO) was synthesized by a modified Hummers' method [42]. In a typical experiment, 2 g of graphite powder was mixed with 150 ml of concentrated sulfuric acid under ice bath (0 °C) and 25 g of potassium permanganate was gradually added under constant stirring and the temperature of the suspension was kept below 20 °C. Then, the suspension was stirred for 4 h followed by diluting with 100 mL of water and the diluted suspension was kept stirring at 50 °C for another 4 h. The suspension was then further diluted with 500 mL of water and treated with 30% H_2O_2 (30 mL) to reduce the residual permanganate. The resultant solid product was separated by centrifugation and washed with hydrochloric acid and water until pH = 7. Finally, the graphene oxide was vacuum-dried at room temperature. For reduced graphene oxide (rGO) sheets, 100 mg of graphene oxide was dispersed in 400 mL of water and subjected to ultrasonication for 4 h and then refluxed for 24 h at 80 °C with 50 mL of hydrazine hydrate to facilitate the reduction.

2.2.4 Synthesis of 2D/1D/2D g-C_3N_4/CdS/rGO ternary nano-composite. Initially, the binary g-C_3N_4/CdS composite was synthesized according to the following procedure. The synthesized g-C_3N_4 nanosheets were dispersed in methanol/water (1:1 volume ratio) solution and subjected to ultrasonication for 30 min and a calculated amount of CdS nanorods was added to the dispersion and ultrasonicated for another 30 min. Then, the suspension was stirred for 12 h under magnetic stirrer at room temperature. Subsequently, the suspension was collected by centrifugation, washed with water and ethanol, and then dried at 80 °C overnight. Finally, the product was heated at 300 °C for 2 h under N_2 atmosphere. A series of g-C_3N_4/CdS composites were synthesized with different weight percentage of CdS to g-C_3N_4, namely 5, 10, 15 and 20 wt.%.

To obtain the g-C_3N_4/CdS/rGO ternary nano-composites, 1 wt.% of rGO (with respect to weight of g-C_3N_4/CdS composites) was mixed in methanol/water (1:1 volume ratio) solution and ultrasonicated for 1 h. After that, the above synthesized g-C_3N_4/CdS powder was added to the suspension and ultrasonicated for 30 min to form a uniform dispersion. After continuous stirring for 3 h, the suspension was collected by centrifugation and washed with water and ethanol, and then dried at 80 °C overnight. A series of g-C_3N_4/CdS/rGO ternary nano-composites with 1 wt.% rGO and 5, 10, 15 and 20 wt% CdS to g-C_3N_4 were synthesized and denoted as CCG-5, CCG-10, CCG-15 and CCG-20, respectively. The binary g-C_3N_4/rGO composite was obtained under the same experimental conditions, but with the addition of g-C_3N_4 rather than g-C_3N_4/CdS.

2.3 Material characterization

Powder X-ray diffraction (XRD) measurements were performed on a Bruker D8-Advance X-ray diffractometer (Germany) with Cu K_α radiation (λ = 1.5418 Å). The photoluminescence (PL) spectra of the samples were recorded using a steady state spectrofluorometer (FLUOROLOG-3-TAU, Jobin Yvon, France) at an excitation wavelength of 365 nm. PL lifetime data collected on Edinburgh Photonics FLS 980 using pico to nanosecond pulsed LED light sources at an excitation wavelength of 380 nm. The surface morphology and chemical composition of the samples were analyzed by field emission scanning electron microscopy (FESEM, JEM-2100F, JEOL, Japan) coupled with energy dispersive X-ray (EDX) spectrometry. UV−visible diffuse reflectance spectra (UV−vis DRS) of samples were obtained on a UV-3600, Shimadzu (UV−vis NIR spectrophotometer) with an integrating sphere, and $BaSO_4$ as the reference material. Transmission electron microscopy (TEM) and high-resolution TEM (HRTEM) images were taken using a FEI Tecnai G^2 transmission electron microscope at an acceleration voltage of 200 kV. X-ray photoelectron spectroscopy (XPS) measurements were conducted on a Kratos Axis ULTRA system incorporating a 165 mm hemispherical electron energy analyzer. Thermogravimetric analysis (TGA) was carried out on a PerkinElmer Pyris Diamond TGA/DTA system in nitrogen atmosphere at a heating rate of 10 °C min^{-1}.

2.4 Photocatalytic activity test

The photocatalytic hydrogen production experiments were performed in a 250 mL quartz photoreactor at ambient temperature and atmospheric pressure, and the outlet of the reactor was sealed with a silicone rubber septum. A 300 W Xe arc lamp through a UV-cutoff filter ($\lambda \geq 420$ nm), which was positioned 15 cm away from the photoreactor, served as the light source to trigger the photocatalytic reaction. In a typical photocatalytic experiment, 50 mg of photocatalyst was suspended in an aqueous solution (100 mL) containing 10 vol.% triethanolamine as a sacrificial electron donor. 0.5 wt % Pt co-catalyst was loaded on the surface of the catalyst by the *in situ* photo-deposition method using hexachloroplatinic acid (H_2PtCl_6) as the precursor. Prior to irradiation, suspensions of the photocatalysts were dispersed by an ultrasonic bath and nitrogen was bubbled through the reaction system for 30 min to completely remove the dissolved oxygen and to ensure the anaerobic conditions. During irradiation, continuous magnetic stirring was applied to ensure homogeneity of the suspension and to eliminate sedimentation. A 500 µL portion of gas was sampled intermittently through the septum, and hydrogen was analyzed by a gas chromatograph (Shimadzu Tracera GC-2010 Plus, with He as a carrier gas and a Barrier Ionization Detector).

The apparent quantum efficiency (QE) for H_2 generation was measured using a 420 nm band-pass filter. The average intensity of irradiation was measured as 25 mW cm^{-2} and the irradiation area was controlled as 5 cm^2. The number of incident photons and the apparent quantum efficiency were estimated by using the following equations.

$$\text{Number of incident photons} = \frac{E\lambda}{hc}$$

$$\text{QE (\%)} = \frac{\text{the no of reacted electrons}}{\text{the no of incident photons}} \times 100$$

$$= \frac{\text{the no of evolved } H_2 \text{ molecules } \times 2}{\text{the no of incident photons}} \times 100$$

2.5 Photoelectrochemical measurements

The photoelectrochemical measurements were performed on a CHI 660B electrochemical workstation using a standard three-electrode system at room temperature. The synthesized photocatalyst, a Ag/AgCl (in saturated KCl), and a Pt wire were used as the working electrode, the reference electrode, and the counter electrode, respectively. The photocurrent response of the photocatalysts was investigated for several on-off cycles of irradiation by a 300 W Xe arc lamp and Na_2SO_4 (0.1 M) was used as the electrolyte solution. The working electrode was fabricated as follows: 20 mg of photocatalyst powder was mixed with 0.5 mL of water, and 0.05 mL of Liquion solution was added to make a slurry. The slurry was then spread on a 2 × 1 cm^2 indium−tin oxide (ITO) glass substrate with an active area of about 0.5 cm^2 and dried at 120 °C for 30 min.

3. Results and discussion

Initially we had synthesized the g-C_3N_4/CdS/rGO ternary nano-composite by using a direct method by dispersing the calculated amounts of g-C_3N_4, CdS and rGO in the methanol/water solution. In this case, all the three components were found to be randomly oriented and no proper interfaces were seen to have been formed between g-C_3N_4, CdS and rGO. Additionally, self aggregation of CdS nanorods was also noted to be very high and the corresponding hydrogen output was found to be low. Therefore, to get sandwiched g-C_3N_4/CdS/rGO heterojunctions a facile wet-chemical method with specific strategy was used wherein a two step sequential process was used.

3.1 Formation of g-C_3N_4/CdS/rGO dual-interface nano-composites

In the present study, g-C_3N_4/CdS/rGO dual-interface nano-composites are synthesized by a facile wet-chemical method. Initially, g-C_3N_4 nanosheets are synthesized by liquid exfoliation of the bulk g-C_3N_4 in water. Then, CdS nanorods which are synthesized by the hydrothermal method are added to the ultrasonically dispersed g-C_3N_4 nanosheets. In this process, CdS nanorods are strongly anchored on the surface of g-C_3N_4 nanosheets as shown in Scheme 1. The synthesized binary g-C_3N_4/CdS composites are then mixed to the rGO suspension. Then the CdS nanorods on the surface of g-C_3N_4 are almost covered by rGO sheets and sandwiched between g-C_3N_4 and rGO sheets to form g-C_3N_4/CdS/rGO ternary heterojunctions. Moreover, by using this synthetic process, dispersion of CdS nanorods could be controlled between g-C_3N_4 and rGO to get strong dual-interfaces between g-C_3N_4, CdS and rGO.

3.2 Characterizations of the g-C_3N_4/CdS/rGO dual-interface nano-composites

To estimate the CdS nanorods content in the final products, TGA was performed on the synthesized dual-interface composite under N_2 atmosphere from room temperature to 800 °C at a heating rate of 10 °C min $^{-1}$. As shown in Fig. S1, the decomposition of g-C_3N_4 starts at 550 °C and is completed at ∼710 °C, which can be identified with the burning of g-C_3N_4 [43]. The weight loss region could be seen in the temperature range of 550–700 °C for the g-C_3N_4/CdS/rGO composites, which is similar to the combustion temperature range of the pure g-C_3N_4. The contents of CdS in the composites could be easily estimated from the remainder weight after heating the samples over 800 °C. The residual weight fractions of the different nanocomposites (CCG-5, CCG-10, CCG-15, and CCG-20) were found to be 5.1, 9.6, 13.9 and 21.4 wt.%, which are identified as the contents of CdS in different g-C_3N_4/CdS/rGO composites.

The crystal structure and phase composition of the synthesized samples were investigated by using X-ray diffraction (XRD). The typical XRD patterns of g-C_3N_4, rGO, CdS, and g-C_3N_4/CdS/rGO composites are shown in Fig. 1. In pure g-C_3N_4 pattern, the strong diffraction peak at 27.6° with a *d* spacing of 0.326 nm reflects the characteristic interlayer-stacking of the conjugated aromatic system, which is representative of graphitic materials, while the small peak at 13.1° represents the in-plane structural packing motif corresponding to a *d* spacing of 0.672 nm [17,27]. For bare rGO, the characteristic peak at 25.8° corresponding to the (002) plane can be attributed to the reduction of graphene oxide and the disordered stacking of rGO, and the other with a much weaker intensity at 43.2° corresponds to the (100) plane [44]. The g-C_3N_4/rGO sample exhibits a similar XRD pattern as that of pure g-C_3N_4 but with low intensity, suggesting that the incorporation of rGO sheets has little influence on the phase structure of g-C_3N_4. The pure CdS sample displays major diffraction peaks at 2θ values of 24.8°, 26.5°, 28.3°, 36.7°, 43.9°, 48.0°, and 52.2° corresponding to the crystalline planes of (100), (002), (101), (102), (110), (103) and (112), respectively, which can be indexed to the hexagonal phase of CdS (JCPDS: 41-1049). The g-C_3N_4/CdS composite exhibits the diffraction peaks corresponding to both g-C_3N_4 and CdS, reflecting the existence of two phases. In addition, for the dual-interface g-C_3N_4/CdS/rGO composites, their XRD patterns exhibit characteristic diffraction peaks of both g-C_3N_4 and CdS crystalline phases, and the peak intensity of the CdS nanorods gradually increases with the increasing CdS content in the composite. As expected, no diffraction hump corresponding to rGO can be discerned in the XRD pattern of g-C_3N_4/CdS/rGO composites, due to its low content. However, the presence of rGO sheets in the g-C_3N_4/CdS/rGO composites can be easily evidenced by UV−vis DRS and XPS analyses, as discussed later.

Fig. 2 shows the UV-vis diffuse reflectance spectra of the synthesized pure g-C_3N_4, rGO, CdS, and binary and ternary composites. As shown in Fig. 2, the absorption edges of pure g-C_3N_4 and CdS are located around 450 and 520 nm, corresponding to the band gap energies of 2.75 and 2.4 eV, respectively. Interestingly, the absorption spectra of g-C_3N_4/CdS and g-C_3N_4/CdS/rGO nano-composites exhibit two-stage absorption edges that are distinct from those of either g-C_3N_4 or CdS, which is in good agreement with the phenomenon observed in other heterojunctions reported in the literature [45-47]. Moreover, the absorption edge slightly red-shifts with increasing intensity when the content of CdS is increased from 5 to 20 wt.%. This result clearly brings out the formation of strong interfaces between g-C_3N_4 and CdS rendering an impact on the electronic states. Besides, the rGO loading enhances the light absorption over the entire range of wavelengths investigated, which is due to the characteristic behavior of rGO in the g-C_3N_4/rGO and g-C_3N_4/CdS/rGO nano-composites [40,48]. It is more interesting that all the rGO containing composites show almost the same absorption tail in the visible region (550 to 800 nm), which further confirms the equal content of rGO in the composites. The decreased band gap energies and enhanced visible-light absorption of the ternary dual-interface heterostructures can therefore provide more photogenerated electrons and holes, which would contribute to the enhanced photocatalytic activity.

The morphologies of the synthesized samples were examined by field-emission scanning electron microscopy (FE-SEM) and transmission electron microscopy (TEM). The pure g-C_3N_4 material clearly exhibits a two-dimensional (2D) thin layered structure (Fig. S2a in the Supplementary Information) composed of numerous randomly organized nanosheets, which indicates the successful exfoliation of g-C_3N_4 nanosheets from its bulk counterparts. It can be seen that the morphology of CdS is in the form of well crystallized 1D nanorods with lengths of

1−2 μm and diameters of about 40 nm (Fig. S2b). As shown in Fig. S2c, rGO has a 2D nanosheet structure with many thin wrinkles on the surface and these wrinkles indicate its ultrathin thickness. For the g-C_3N_4/CdS composite, several CdS nanorods are well anchored on the surface of g-C_3N_4 (Fig. 3), and almost all nanorods are in direct contact with the g-C_3N_4. Interestingly, after incorporating rGO with the g-C_3N_4/CdS composite, the deposited CdS nanorods are almost sandwiched and closely compacted between g-C_3N_4 and rGO sheets to make a g-C_3N_4/CdS/rGO (2D/1D/2D) ternary dual-interface nano-composite. Fig. S3 b–e show the elemental mapping images of a relatively homogeneous distribution of C, N, Cd and S, which further confirms the composition of the g-C_3N_4, CdS and rGO in the ternary materials system.

In order to further analyze the interaction between g-C_3N_4, CdS, and rGO in the g-C_3N_4/CdS/rGO nano-composite, TEM studies were conducted. The CdS nanorods are seen to be well sandwiched between the g-C_3N_4 nanosheets and rGO sheets without much aggregation, as shown in Fig. 4a. Besides, the magnified TEM images (Fig. 4b to e) clearly show the strong interactions between g-C_3N_4, CdS, and rGO, and the CdS nanorods are strongly attached to both g-C_3N_4, and rGO sheets. Furthermore, the interplanar distance of 0.67 nm measured out in the HRTEM image (Fig. 4f) is in good agreement with the (002) plane of the hexagonal phase of CdS [49]. A different kind of lattice fringes with d spacing of 0.325 nm is corresponds to the typical (002) interlayer-stacking distance of g-C_3N_4. The morphology studies also revealed that rGO could serve as a support to bind the g-C_3N_4/CdS composite in the dual-interface ternary nano-composite system, which leads to the formation of interfaces between g-C_3N_4, CdS, and rGO, and to favorable photoinduced charge transfer at the interface.

To further confirm the chemical composition and surface chemical state of elements in the g-C_3N_4/CdS/rGO system, X-ray photoelectron spectroscopy (XPS) measurements were conducted.

The survey XPS spectrum of the CCG-10 photocatalyst reveals the presence of C, N, Cd and S elements (Fig. 5a). The additional O 1s peak at 532 eV was ascribed to –OH groups at the surface resulting from the surface absorbed water [50,51]. The high-resolution C 1s spectrum can be fitted to three different peaks, located at the binding energies of 284.7, 286.1, and 288.2 eV (Fig. 5b). The main peak at 288.2 eV is attributed to the sp^2-hybridized C in the N-containing aromatic ring (N−C═N), which represents the major carbon environment in g-C_3N_4 [21,52]. The peak at 284.7 eV is assigned to the sp^2 C−C bonds of graphene [53], and the small peak located at 286.1 eV could be assigned to sp^3-coordinated carbon bonds from the defects on the g-C_3N_4 surface [54], which clearly indicates the existence of rGO and g-C_3N_4 in the dual-interface ternary nano-composite system. Moreover, the high resolution N 1s spectra in Fig. 5c were deconvoluted into three different peaks centering at 398.5, 399.6, and 401.4 eV. The dominant peak at a binding energy of 398.5 eV can be ascribed to the sp^2-hybridized nitrogen in triazine rings (C−N═C), and the peak at 399.6 eV corresponds to the bridged tertiary nitrogen N−$(C)_3$ groups [55,56]. Both these N 1s species in C−N═C (398.5 eV) and N–$(C)_3$ (399.6 eV) groups, together with sp^2-hybridized C 1s (N−C═N, 288.2 eV), are considered to compose tri-*s*-triazine motifs as building blocks for g-C_3N_4. The weak peak located at 401.4 eV can be assigned to amino functional groups having a hydrogen atom (C–N–H), which plays an important role in the covalent link between g-C_3N_4 and the rGO [40,55]. In addition, the binding energies of Cd 3d are determined to be 404.9 and 411.7 eV (Fig. 5c), which belong to Cd $3d_{5/2}$ and Cd $3d_{3/2}$ of Cd^{2+} in CdS nanorods, respectively [57]. The S 2p spectrum (Fig. 5d) shows peaks with the binding energies of 161.2 eV (S $2p_{3/2}$) and 162.5 eV (S $2p_{1/2}$), which are ascribed to S^{2-} in CdS [58]. All the above characterization results unambiguously confirm the formation of 2D/1D/2D g-C_3N_4/CdS/rGO dual interface nano-composite.

3.3 Photocatalytic hydrogen generation

Photocatalytic hydrogen generation activities of the synthesized g-C_3N_4/CdS/rGO composites were evaluated under visible-light irradiation using triethanolamine as the sacrificial reagent to quench photogenerated holes. According to the control experiments, no obvious H_2 production was detected in the absence of either light or catalyst, suggesting that H_2 was truly generated in the photocatalytic process. Fig. 6a displays the variation in H_2 production with irradiation time over pure g-C_3N_4 and g-C_3N_4/CdS/rGO photocatalytic systems. For comparison, photocatalytic H_2 production activities of bulk g-C_3N_4, and binary g-C_3N_4/rGO and g-C_3N_4/CdS heterojunctions were also conducted. It can be seen that the H_2 production rate is negligible (10.8 μmol h^{-1} g^{-1}) over the bulk g-C_3N_4 (Fig. 6b) due to the low surface area and high recombination rate of photogenerated charge carriers, and the rate of H_2 production over g-C_3N_4 nanosheets reaches 108.5 μmol h^{-1} g^{-1} after the liquid exfoliation of bulk g-C_3N_4. In the presence of a small amount (1 wt.%) of rGO sheets, the H_2 production activity of the g-C_3N_4 nanosheets is significantly improved. Besides, the binary g-C_3N_4/CdS heterojunction (with 10 wt.% CdS) shows a good photocatalytic H_2 production (1982.7 μmol h^{-1} g^{-1}), which is much higher than that of pure g-C_3N_4 nanosheets and binary g-C_3N_4/rGO composite. More remarkably, after adding 1 wt.% of rGO sheets to the g-C_3N_4/CdS heterojunctions, the photocatalytic H_2 production activity was remarkably enhanced. In particular, the CCG-10 sample (which contains ~10 wt.% CdS and 1 wt.% rGO) exhibits the highest H_2 production rate of ~4800 μmol h^{-1} g^{-1}, which is almost eleven times higher than that for the binary g-C_3N_4/rGO (412.8 μmol h^{-1} g^{-1}) and more than 2 times that for the binary g-C_3N_4/CdS heterojunction (1982.7 μmol h^{-1} g^{-1}) systems.

Additionally, the H_2 production activity of the present ternary systems was compared with that of pure CdS, CdS/rGO (1 wt.% of rGO), and physical mixture of binary CN/rGO and

CdS/rGO composites, and results are presented in the supplementary material (Fig. S4). Evidently, all the four dual-interface nano-composite photocatalysts exhibit superior photocatalytic activities than all the other pure and binary photocatalysts. However, when the CdS nanorods content increased beyond 10 wt.% in the ternary nano-composite, a decrease in the H_2 production rate was observed. This phenomenon can be explained as follows: (1) the optimum CdS nanorods content (10 wt.%) causes their good dispersion on the surface of g-C_3N_4 nanosheets, which favors the efficient separation and transfer of the photogenerated charge carriers, and (2) at a very high content of CdS nanorods, there is a good chance of self aggregation, hence, the existence of g-C_3N_4/CdS heterojunction will be in jeopardy, leading to a lower H_2 production rate. Therefore, an appropriate amount of CdS is crucial for optimizing the photocatalytic activity of dual-interface ternary nano-composite. In the present study, the g-C_3N_4/CdS/rGO photocatalytic system containing optimum CdS content (10 wt.%) exhibits the highest photocatalytic activity with an apparent quantum efficiency (QE) of 11.1% measured at 420 nm. Moreover, the photocatalytic efficiency of the present g-C_3N_4/CdS/rGO system is much higher than those of previously reported g-C_3N_4/rGO [40], CdS QDs/g-C_3N_4 [39], CdS/g-C_3N_4 core/shells [59], and MoS_2/mpg-C_3N_4 [60] composites.

3.4 Photocatalytic mechanism

In order to investigate the photocatalytic mechanism for the enhanced photocatalytic H_2 production of the g-C_3N_4/CdS/rGO dual-interface ternary system, photoluminescence (PL) spectroscopy measurements were performed. In general, PL measurements are often used to qualitatively investigate the transfer and separation efficiency of photogenerated electrons and holes in semiconductor materials, since the PL emission arises from the recombination of charge carriers [27,30]. Fig. 7a shows the PL spectra of the synthesized pure g-C_3N_4, and the binary and ternary nano-composites recorded at room temperature with an excitation wavelength of 365 nm. It can be seen that introducing rGO into the g-C_3N_4 network reduces the PL intensity significantly as compared with that of pure g-C_3N_4, indicating the effective separation of photogenerated charge carriers. In addition, the binary g-C_3N_4/CdS composite exhibits more quenching of the PL emission as compared to g-C_3N_4/rGO, which is due to the efficient charge transfer between g-C_3N_4 and CdS, thus leading to the reduced recombination of photogenerated electron–hole pairs. More remarkably, the intensity of PL signal for the g-C_3N_4/CdS/rGO ternary nano-composite is much lower than that for pure g-C_3N_4 and binary heterojunctions, and least PL signal is observed for the CCG-10 photocatalyst, which is completely consistent with the result of photocatalytic H_2 production performance. This indicates that the dual-interface ternary nano-composite has a lower recombination rate of charge carriers under visible-light irradiation, which may be due to the fact that the electrons are transferred from the CB of g-C_3N_4 to the CB of CdS, and then transfer to rGO sheets, preventing a direct recombination of electrons and holes [40,50,61]. Therefore, the greater separation of photogenerated electrons and holes contributes to the improved photocatalytic performance of g-C_3N_4/CdS/rGO dual-interface ternary system.

Time-resolved fluorescence spectroscopy was used to study the roles of interface on the dynamics of the photogenerated electron-hole pairs as shown in Fig. 7b. A “biexponential” function model was applied to fit the decay curves as follows:

$$Fit = A + A_1 e^{\left(\frac{-t}{\tau_1}\right)} + A_2 e^{\left(\frac{-t}{\tau_2}\right)}$$

Where $A_{n\,(=1,2,3)}$ = constant, and t = time

The shorter decay life-time (τ_1) and longer decay life-time (τ_2) corresponds to the non-radiative and radiative relaxation process, respectively. The radiative relaxation process is directly related to the direct recombination of photogenerated holes and electrons. The average life time of charge carrier (τ) can be calculated from the equation as given below:

$$\tau = \frac{B_1\tau_1 + B_2\tau_2}{B_1 + B_2}$$

in which B_1 and B_2 are relative to percentages of non-radiative and radiative component, respectively. Table 1 shows the fitted parameters of the time-resolved fluorescence decay spectra of all three samples. The parameter (χ^2) values in the table shows the goodness of fit. The average lifetime (τ) is 2.59, 5.20, 4.58 and 10.34 ns for pure g-C_3N_4, g-C_3N_4/CdS, g-C_3N_4/rGO and g-C_3N_4/CdS/rGO, respectively. It can be clearly seen that the g-C_3N_4/CdS/rGO ternary nano-composite showed a highest charge carrier life-time which is 4, 2 and 2.3 times higher than pure g-C_3N_4, g-C_3N_4/CdS and g-C_3N_4/rGO, respectively. This confirmed that formation of extended interface at the g-C_3N_4/CdS/rGO ternary nano-composite which slows down the electron–hole pair recombination, due to the well-matched overlapping band-structures and the intimate interfacial contact [62,63]. These results clearly demonstrate that the prolonged lifetime of the charge carriers in ternary system will play an important role in improving the probability of their participation in photocatalytic reactions before recombination.

To give further evidence to support the enhanced charge carrier separation efficiency of ternary system, the transient photocurrent measurements were recorded which can provide the strong evidence to demonstrate the light response and interfacial charge transfer dynamics between the composite semiconductors [35,45]. Fig. 8 shows a comparison of the photocurrent-time (I-t) curves for pure g-C_3N_4, and the binary and ternary systems with several on-off cycles of intermittent visible-light irradiation. Evidently, the photocurrent response of CCG-10 photocatalyst is several times higher than that of pure g-C_3N_4 and the binary heterojunctions, which can be ascribed to the existence of strong interfaces between three components in the g-C_3N_4/CdS/rGO, where photoinduced electrons and holes could be efficiently separated in space and the photogenerated charge carrier recombination got reduced. As a result, the CCG-10 photocatalyst exhibits higher photocurrent response, which is in good accordance with the effectively reduced recombination of photogenerated electrons and holes from the PL analysis.

Based on the above experimental results, an illustration of possible interface electron transfer behavior and the corresponding photocatalytic H_2 production mechanism is depicted in Fig. 9. Under visible-light illumination, both g-C_3N_4 and CdS are excited to generate the electrons and holes in the CB and VB, respectively. Owing to the well-matched overlapping band structures and closely contacted interfaces, photogenerated electrons in the CB of g-C_3N_4 can be easily transferred to the CB of CdS, and meanwhile, the photoinduced holes on the VB of CdS can migrate to the VB of g-C_3N_4, leading to electron-hole separation. This is also due to the fact that the redox potentials of both CB (E_{CB} = −1.3 eV *vs.* NHE) and VB (E_{VB} = +1.4 eV *vs.* NHE) of g-C_3N_4 are more negative than those of the CB (E_{CB} = −0.5 eV *vs.* NHE) and VB (E_{VB} = +1.9 eV *vs.* NHE) of CdS, respectively [30,39,43,47]. Thereafter, the electrons excited from the CB of CdS together with the rest electrons from the CB of g-C_3N_4 can be directly captured by rGO sheets due to its excellent electronic conductivity, which further leads to minimize the possibility of the recombination of electrons and holes. Subsequently, the captured electrons will accumulate on the Pt nanoparticles (Fig. S5) loaded on the ternary nano-composite and then effectively participate in photocatalytic H_2 production reaction. Besides, the holes at the VB of g-C_3N_4 together with the transferred holes from the VB of CdS can react with triethanolamine (sacrificial reagent) to reduce the electron-hole recombination, and to significantly alleviate the photocorrosion of CdS. It is also worth noting that the strong 2D/1D construction of g-C_3N_4/CdS facilitates the increased interfacial contact area between g-C_3N_4 nanosheets and CdS nanorods, and greater charge transfer rate as compared to that reported in the cases of 0D/2D CdS QDs/ g-C_3N_4 [39] and 2D/0D g-C_3N_4/CdS NPs [64] photocatalysts. Therefore, the synergistic effect of matching the band structure between 2D g-C_3N_4 nanosheets and 1D CdS nanorods, and superior conductivity of 2D rGO sheets together contribute to the enhanced photocatalytic H_2 production activity of the g-C_3N_4/CdS/rGO ternary system. The main reaction steps involved in the photocatalytic H_2 production mechanism under visible-light irradiation are summarized by the following equations.

$$\mathrm{g\!-C_3N_4/CdS/rGO} + \mathrm{h\vartheta}\ (\text{visible light}) \longrightarrow \mathrm{g\!-C_3N_4/CdS}\ (\mathrm{h^+_{VB}} + \mathrm{e^-_{CB}})\ \ (\text{excitation process})$$

$$\mathrm{g\!-C_3N_4/CdS}\ (\mathrm{h^+_{VB}} + \mathrm{e^-_{CB}}) \longrightarrow \mathrm{g\!-C_3N_4(h^+_{VB})}\ /\ \mathrm{CdS}\ (\mathrm{e^-_{CB}})\ (\text{Charge transfer process})$$

$$\mathrm{g\!-C_3N_4(h^+_{VB})} + \mathrm{TEOA} \longrightarrow \mathrm{g\!-C_3N_4} + \mathrm{TEOA^+}\ (\text{holes trapping})$$

$$\mathrm{CdS}\ (\mathrm{e^-_{CB}}) + \mathrm{rGO} \longrightarrow \mathrm{CdS} + \mathrm{rGO}\ (\mathrm{e^-})\ (\text{electron transfer})$$

$$\mathrm{rGO}\ (\mathrm{e^-}) + \mathrm{Pt} \longrightarrow \mathrm{rGO} + \mathrm{Pt}\ (\mathrm{e^-})\ (\text{accumulation of electrons})$$

$$\mathrm{Pt}\ (\mathrm{e^-}) + \mathrm{H_2O/H^+} \longrightarrow \mathrm{Pt} + \mathrm{H_2}\ (\text{gas})\ (\text{hydrogen generation process})$$

Although the excellent photocatalytic activity of the g-C_3N_4/CdS/rGO ternary nano-composite is establish, the long-term stability of the photocatalyst is equally important to examine with regard to practical applications. Thus, the photostability of the optimal g-C_3N_4/CdS/rGO ternary system (CCG-10) for photocatalytic H_2 production was further investigated through five successive runs under the same experimental conditions. Each run was conducted for 4 h and after every run the reaction system was re-evacuated. As shown in Fig. 10, the photocatalytic H_2 production activity of the CCG-10 photocatalyst was retained over more than 90% of its original activity after five successive experimental runs under visible-light irradiation, which indicates the high photostability of the dual-interface ternary nano-composite system during photocatalytic H_2 production reaction. It is also well known that an invincible problem for metal-sulfide photocatalysts in photocatalysis process is their poor stability due to photocorrosion (MS + holes/2h^+ $\longrightarrow$ M^{2+} + S, where M is metal) under light irradiation [59,65]. In contrast, the present ternary nano-composite exhibits remarkable stability even after five cycles under visible-light irradiation. This result clearly demonstrates that CdS nanorods are tightly wrapped (encapsulated) in between g-C_3N_4 and rGO sheets, and strong heterojunctions formed between CdS, g-C_3N_4 and rGO. This ternary system can therefore achieve a greater interfacial charge transfer, which can avoid the photocorrosion of CdS by photogenerated holes, and thus improve the photostability of g-C_3N_4/CdS/rGO during the photocatalytic H_2 production process. XPS and XRD measurements conducted before and after the photocatalytic experiments further confirmed the stability of the ternary nano-composite (CCG-10). As shown in Fig. S4, no significant changes in the binding energies of cadmium and sulfur were observed before and after experiments, indicating that the oxidation state of Cd and S did not change after the reaction. Moreover, the XRD pattern (Fig. S5) of the reused sample also clearly demonstrated that the structural aspects of the CCG-10 photocatalyst did not change after the reaction.

The case of a semiconductor nanocrystal functionally encapsulated with two 2D conducting materials which are functional in their own right is representative of an interesting class of materials that can be engineered for specific applications. This approach allows us to wrap stable functional materials around a corrosive but functionally useful material so as to get enhanced as well as stable performance. A two material single interface system has specific limitations to achieve carrier separation which can be largely lifted if one uses a three material dual-interface system as done in the present work. Moreover the use of a nanostructure as the central component provides the adequate level of porosity for electrolyte ion transport in the case of electrochemical applications. Also, the use of the right electronically and optically chosen materials as the wrapping systems can add further value in terms of driving the photo-generated charges such farther apart. This feature dramatically reduces the residence time of electrons and holes in the centrally placed material by sweeping them towards and into the encapsulating materials, thereby forbidding the redox catalytic activity of the central corrosive material to play out.

4. Conclusions

In summary, we have successfully synthesized sandwich like g-C_3N_4 nanosheet (2D)/ CdS nanorod (1D)/ rGO sheet (2D) dual-interface ternary nano-composite with intimate interfacial contact by a facile wet-chemical method. The ternary system exhibits excellent and much superior photocatalytic H_2 production activity under visible-light irradiation as compared to the pure g-C_3N_4, and the binary g-C_3N_4/rGO and g-C_3N_4/CdS heterojunction photocatalysts. Remarkably, the g-C_3N_4/CdS/rGO ternary heterojunction system containing optimum CdS (~10 wt.%) and rGO (1 wt.%) contents shows the highest photocatalytic H_2 production rate of ~4800 μmol h^{-1} g^{-1}, with an apparent quantum efficiency of 11.1% at 420 nm. In addition, the g-C_3N_4/CdS/rGO is highly photostable even after five successive experimental runs, without any obvious change in the H_2 production rate. The enhancement in both the photocatalytic H_2 production performance and the photostability are mainly assigned to the effective separation and transfer of photoinduced charge carriers at the two intimate interfaces of g-C_3N_4/CdS/rGO ternary nano-composite system, which are attributed to the well-matched overlapping band-structures. The present work thus provides an insight into the design and development of novel multi-dimensional heterojunction photocatalysts for diverse photocatalytic applications.

Acknowledgments

S. T. likes to thank the Director, IISER Pune, for funding postdoctoral fellowship. SBO acknowledges funding support by DST Nanomission.

References

[1] Tong H, Ouyang S, Bi Y, Umezawa N, Oshikiri M, Ye J. Nano-photocatalytic materials: possibilities and challenges. Adv Mater 2012;24:229–51.

[2] Kudo A, Miseki Y. Heterogeneous photocatalyst materials for water splitting. Chem Soc Rev 2009;38:253–78.

[3] Yuan YP, Ruan LW, Barber J, Loo SCJ, Xue C. Hetero-nanostructured suspended photocatalysts for solar-to-fuel conversion. Energy Environ Sci 2014;7:3934–51.

[4] Fujishima A, Zhang X, Tryk DA. Heterogeneous photocatalysis: From water photolysis to applications in environmental cleanup. Int J Hydrogen Energ 2007;32:2664–72.

[5] Chen XB, Shen SH, Guo LJ, Mao SS. Semiconductor-based photocatalytic hydrogen generation. Chem Rev 2010;110:6503–70.

[6] Kelkar SA, Shaikh PA, Pachfule P, Ogale SB. Nanostructured Cd_2SnO_4 as an energy harvesting photoanode for solar water splitting. Energ Environ Sci 2011;5:5681–5.

[7] Biswal M, Deshpande A, Kelkar S, Ogale SB. Water electrolysis with a conducting carbon cloth: subthreshold hydrogen generation and superthreshold carbon quantum dot formation ChemSusChem 2014;7:883–9.

[8] Ye S, Wang R, Wu MZ, Yuan YP. A review on g-C_3N_4 for photocatalytic water splitting and CO_2 reduction. Appl Surf Sci 2015;358:15–27.

[9] Fujishima A, Honda K. Electrochemical photolysis of water at a semiconductor electrode. Nature 1972;238:37–8.

[10] Fang J, Xu L, Zhang Z, Yuan Y, Cao S, Wang Z, et al. Au@TiO_2–CdS ternary nanostructures for efficient visible-light-driven hydrogen generation. ACS Appl Mater Interfaces 2013;5:8088–92.

[11] Bhosale R, Kelkar S, Parte G, Fernandes R, Kothari DC, Ogale SB. $NiS_{1.97}$:a new efficient water oxidation catalyst for photoelectrochemical hydrogen generation. ACS Appl Mater Interfaces 2015;7:20053–60.

[12] Wang G, Huang B, Li Z, Lou Z, Wang Z, Dai Y, et al. Synthesis and characterization of ZnS with controlled amount of S vacancies for photocatalytic H_2 production under visible light. Sci Rep 2015;5:8544.

[13] Yu J, Qi L, Jaroniec M. Hydrogen production by photocatalytic water splitting over Pt/TiO_2 nanosheets with exposed (001) facets. J Phys Chem C 2010;114:13118–25.

[14] Sheikh A, Yengantiwar A, Deo M, Kelkar S, Ogale SB. Near-field plasmonic functionalization of light harvesting oxide–oxide heterojunctions for efficient solar photoelectrochemical water splitting: the AuNP/$ZnFe_2O_4$/ZnO system. Small 2013;9:2091–6.

[15] Yu H, Ouyang S, Yan S, Li Z, Yu T, Zou Z. Sol–gel hydrothermal synthesis of visible-light-driven Cr-doped $SrTiO_3$ for efficient hydrogen production. J Mater Chem 2011;21:11347–51.

[16] Kanhere P, Zheng J, Chen Z. Visible light driven photocatalytic hydrogen evolution and photophysical properties of Bi^{3+} doped $NaTaO_3$. Int J Hydrogen Energ 2012;37:4889–96.

[17] Wang X, Maeda K, Thomas A, Takanabe K, Xin G, Carlsson JM, et al. A metal-free polymeric photocatalyst for hydrogen production from water under visible light. Nat Mater 2009;8:76–80.

[18] Cao S, Low J, Yu J, Jaroniec M. Polymeric photocatalysts based on graphitic carbon nitride. Adv Mater 2015;27:2150–76.

[19] Wang S, Li C, Wang T, Zhang P, Li A, Gong J. Controllable synthesis of nanotube-type graphitic C_3N_4 and their visible-light photocatalytic and fluorescent properties. J Mater Chem A 2014;2:2885–90.

[20] Yuan YP, Yin LS, Cao SW, Gu LN, Xu GS, Du P, et al. Microwave-assisted heating synthesis: a general and rapid strategy for large-scale production of highly crystalline g-C_3N_4 with enhanced photocatalytic H_2 production. Green Chem 2014;16:4663–68.

[21] Wang Y, Wang X, Antonietti M. Polymeric graphitic carbon nitride as a heterogeneous organocatalyst: from photochemistry to multipurpose catalysis to sustainable chemistry. Angew Chem Int Ed 2012;51:68–89.

[22] Suryawanshi A, Dhanasekaran P, Mhamane D, Kelkar S, Patil S, Gupta N, Ogale SB. Doubling of photocatalytic H_2 evolution from g-C_3N_4 via its nanocomposite formation with multiwall carbon nanotubes: electronic and morphological effects. Int J Hydrogen Energ 2012;37:9584–9.

[23] Zheng Y, Jiao Y, Chen J, Liu J, Liang J, Du A, et al. Nanoporous graphitic-C_3N_4@carbon metal-free electrocatalysts for highly efficient oxygen reduction. J Am Chem Soc 2011;133:20116–9.

[24] Zhang J, Zhang G, Chen X, Lin S, Mçhlmann L, Dołega G, et al. Co-monomer control of carbon nitride semiconductors to optimize hydrogen evolution with visible light. Angew Chem Int Ed 2012;51:3183–7.

[25] Wang R, Gu L, Zhou J, Liu X, Teng F, Li C, et al. Quasi-polymeric metal–organic framework UiO-66/g-C_3N_4 heterojunctions for enhanced photocatalytic hydrogen evolution under visible light irradiation. Adv Mater Interfaces 2015;2:1500037.

[26] Huang ZF, Song J, Pan L, Wang Z, Zhang X, Zou JJ, et al. Carbon nitride with simultaneous porous network and O-doping for efficient solar-energy-driven hydrogen evolution. Nano Energ 2015;12:646–56.

[27] Tonda S, Kumar S, Kandula S, Shanker V. Fe-doped and -mediated graphitic carbon nitride nanosheets for enhanced photocatalytic performance under natural sunlight. J Mater Chem A 2014;2:6772–80.

[28] Liu G, Niu P, Sun C, Smith CS, Chen ZG, Lu GM, et al. Unique electronic structure induced high photoreactivity of sulfur-doped graphitic C_3N_4. J Am Chem Soc 2010;132:11642–8.

[29] Maeda K, Wang X, Nishihara Y, Lu D, Antonietti M, Domen K. Photocatalytic activities of graphitic carbon nitride powder for water reduction and oxidation under visible light. J Phys Chem C 2009;113:4940–7.

[30] Kumar S, Surendar T, Baruah A, Shanker V. Synthesis of a novel and stable g-C_3N_4–Ag_3PO_4 hybrid nanocomposite photocatalyst and study of the photocatalytic activity under visible light irradiation. J Mater Chem A 2013;1:5333–40.

[31] Yuan YP, Xu WT, Yin LS, Cao SW, Liao YS, Tng YQ, et al. Large impact of heating time on physical properties and photocatalytic H_2 production of g-C_3N_4 nanosheets synthesized through urea polymerization in Ar atmosphere. Int J Hydrogen Energ 2013;38:13159–63.

[32] Li C, Wang S, Wang T, Wei Y, Zhang P, Gong J. Monoclinic porous $BiVO_4$ networks decorated by discrete g-C_3N_4 nano-islands with tunable coverage for highly efficient photocatalysis. Small 2014;10:2783–90.

[33] Zhao Z, Sun Y, Dong F, Graphitic carbon nitride based nanocomposites: a review. Nanoscale 2015;7:15–37.

[34] Lei J, Chen Y, Shen F, Wang L, Liu Y, Zhang J. Surface modification of TiO_2 with g-C_3N_4 for enhanced UV and visible photocatalytic activity. J Alloys Compd 2015;631:328–34.

[35] Wang YJ, Shi R, Lin J, Zhu YF. Enhancement of photocurrent and photocatalytic activity of ZnO hybridized with graphite-like C_3N_4. Energy Environ Sci 2011;4:2922–9.

[36] Xu X, Liu G, Randorn C, Irvine JTS. g-C_3N_4 coated $SrTiO_3$ as an efficient photocatalyst for H_2 production in aqueous solution under visible light irradiation. Int J Hydrogen Energ 2011;36:13501–7.

[37] Huang L, Xu H, Li Y, Li H, Cheng X, Xia J, et al. Visible-light-induced WO_3/g-C_3N_4 composites with enhanced photocatalytic activity. Dalton Trans 2013;42:8606–16.

[38] She X, Xu H, Wang H, Xia J, Song Y, Yan J, et al. Controllable synthesis of CeO_2/g-C_3N_4 composites and their applications in the environment. Dalton Trans 2015;44:7021–31.

[39] Cao SW, Yuan YP, Fang J, Shahjamali MM, Boey FYC, Barber J, et al. In-situ growth of CdS quantum dots on g-C_3N_4 nanosheets for highly efficient photocatalytic hydrogen generation under visible light irradiation. Int J Hydrogen Energ 2013;38:1258–66.

[40] Xiang Q, Yu J, Jaroniec M. Preparation and enhanced visible-light photocatalytic H_2-production activity of graphene/C_3N_4 composites. J Phys Chem C 2011;115:7355–63.

[41] Williams G, Seger B, Kamat PV. TiO_2-graphene nanocomposites UV-assisted photocatalytic reduction of graphene oxide. A*CS Nano* 2008;2:1487–91.

[42] Marcano DC, Kosynkin DV, Berlin JM, Sinitskii A, Sun ZZ, Slesarev A, et al. Improved synthesis of graphene oxide. ACS Nano 2010;4:4806–14.

[43] Kumar S, Surendar T, Kumar B, Baruah A, Shanker V. Synthesis of magnetically separable and recyclable g-C_3N_4–Fe_3O_4 hybrid nanocomposites with enhanced photocatalytic performance under visible-light irradiation. J Phys Chem C 2013;117:26135–43.

[44] Gunjakar JL, Kim IY, Lee JM, Lee NS, Hwang SJ. Self-assembly of layered double hydroxide 2D nanoplates with graphene nanosheets: an effective way to improve the photocatalytic activity of 2D nanostructured materials for visible light-induced O_2 generation. Energy Environ Sci 2013;6:1008–17.

[45] Jiang D, Li J, Xing C, Zhang Z, Meng S, Chen M. Two-dimensional $CaIn_2S_4$/g-C_3N_4 heterojunction nanocomposite with enhanced visible-light photocatalytic activities: interfacial engineering and mechanism insight. *ACS Appl Mater Interfaces* 2015;7:19234–42.

[46] Zang Y, Li L, Zuo Y, Lin H, Li G, Guan X. Facile synthesis of composite g-C_3N_4/WO_3: a nontoxic photocatalyst with excellent catalytic activity under visible light. RSC Adv 2013;3:13646–50.

[47] Yuan J, Wen J, Zhong Y, Li X, Fang Y, Zhang S, et al. Enhanced photocatalytic H_2 evolution over noble-metal-free NiS cocatalyst modified CdS nanorods/g-C_3N_4 heterojunctions. J Mater Chem A 2015;3:18244–55.

[48] Hou Y, Wen Z, Cui S, Guo X, Chen J. Constructing 2D porous graphitic C_3N_4 nanosheets/nitrogen-doped graphene/layered MoS_2 ternary nanojunction with enhanced photoelectrochemical activity. Adv Mater 2013;25:6291–7.

[49] Jang JS, Joshi UA, Lee JS. Solvothermal synthesis of CdS nanowires for photocatalytic hydrogen and electricity production. *J Phys Chem C,* 2007;111:13280–7.

[50] Wang L, Ding J, Chai Y, Liu Q, Ren J, Liu X, et al. CeO_2 nanorod/g-C_3N_4/N-rGO composite: enhanced visible-light-driven photocatalytic performance and the role of N-rGO as electronic transfer media. Dalton Trans 2015;44 11223–34.

[51] Liang Q, Li Z, Yu X, Huang ZH, Kang F, Yang QH. Macroscopic 3D porous graphitic carbon nitride monolith for enhanced photocatalytic hydrogen evolution. Adv Mater 2015;27:4634–9.

[52] Vinu A. Two-dimensional hexagonally-ordered mesoporous carbon nitrides with tunable pore diameter surface area and nitrogen content. Adv Funct Mater 2008;18:816–27.

[53] Sun Y, Li C, Xu Y, Bai H, Yao Z, Shi G. Chemically converted graphene as substrate for immobilizing and enhancing the activity of a polymeric catalyst. Chem Commun 2010;46:4740–2.

[54] Zhang G, Zhang J, Zhang M, Wang X. Polycondensation of thiourea into carbon nitride semiconductors as visible light photocatalysts. J Mater Chem 2012;22:8083–91.

[55] Li Y, Wei X, Li H, Wang R, Feng J, Yun H, et al. Fabrication of inorganic–organic core–shell heterostructure: novel CdS@g-C_3N_4 nanorod arrays for photoelectrochemical hydrogen evolution. RSC Adv 2015;5:14074–80.

[56] Thomas A, Fischer A, Goettmann F, Antonietti M, Muller JO, Schlogl R, et a. Graphitic carbon nitride materials: variation of structure and morphology and their use as metal-free catalysts. J Mater Chem 2008;18:4893–908.

[57] Xiao FX, Miao J, Liu B. Layer-by-layer self-assembly of CdS quantum dots/graphene nanosheets hybrid films for photoelectrochemical and photocatalytic applications. J Am Chem Soc 2014;136:1559–69.

[58] Zhang LJ, Zheng R, Li S, Liu BK, Wang DJ, Wang LL, et al. Enhanced photocatalytic H_2 generation on cadmium sulfide nanorods with cobalt hydroxide as cocatalyst and insights into their photogenerated charge transfer properties. ACS Appl Mater Interfaces 2014;6:13406–12.

[59] Zhang J, Wang Y, Jin J, Zhang J, Lin Z, Huang F, et al. Efficient visible-light photocatalytic hydrogen evolution and enhanced photostability of core/shell CdS/g-C_3N_4 nanowires. ACS Appl Mater Interfaces 2013;5:10317–24.

[60] Hou Y, Laursen AB, Zhang J, Zhang G, Zhu Y, Wang X, et al. Layered nanojunctions for hydrogen-evolution catalysis. Angew Chem Int Ed 2013;52:3621–5.

[61] Pawar RC, Khare V, Sunyong Lee C. Hybrid photocatalysts using graphitic carbon nitride/cadmium sulfide/reduced graphene oxide (g-C_3N_4/CdS/RGO) for superior photodegradation of organic pollutants under UV and visible light. Dalton Trans 2014;43:12514–27.

[62] Chen J, Shen S, Wu P, Guo L. Nitrogen-doped CeO_x nanoparticles modified graphitic carbon nitride for enhanced photocatalytic hydrogen production. Green Chem 2015;17:509–17.

[63] Padhi DK, Parida K, Singh SK. Facile fabrication of RGO/N-GZ mixed oxide nanocomposite for efficient hydrogen production under visible light. J Phys Chem C 2015;119:6634−46.

[64] Fu J, Chang B, Tian Y, Xi F, Dong X. Novel C_3N_4–CdS composite photocatalysts with organic–inorganic heterojunctions: in situ synthesis exceptional activity high stability and photocatalytic mechanism. J Mater Chem A 2013;1:3083–90.

[65] Lu M, Pei Z, Weng S, Feng W, Fang Z, Zheng Z, et al. Constructing atomic layer g-C_3N_4–CdS nanoheterojunctions with efficiently enhanced visible light photocatalytic activity. Phys Chem Chem Phys 2014;16:21280–8.

Figure captions

Scheme 1 Schematic representation of the synthesis of g-C_3N_4/CdS/rGO dual-interface nano-composite system.

Fig. 1 XRD patterns of the synthesized g-C_3N_4, CdS, rGO, g-C_3N_4/rGO, g-C_3N_4/CdS and g-C_3N_4/CdS/rGO samples.

Fig. 2 UV−vis diffuse reflectance spectra of g-C_3N_4, CdS, rGO, g-C_3N_4/rGO, g-C_3N_4/CdS and g-C_3N_4/CdS/rGO heterojunctions.

Fig. 3 FESEM images of (a) g-C_3N_4/CdS (b) CCG-10 heterojunctions (The highlighted area represents the direct contact and sandwich nature of CdS nanorods in g-C_3N_4/CdS and CCG-10, respectively).

Fig. 4 TEM image (a), and magnified TEM images (b to e) of CCG-10 ternary heterojunction. (f) HRTEM image of the CCG-10 ternary heterojunction.

Fig. 5 XPS spectra of CCG-10 ternary heterojunction; (a) survey spectrum, (b) C 1s, (c) N 1s and Cd 3d, and (d) S 2p spectra.

Fig. 6 (a) Photocatalytic H_2 generation over various photocatalysts under visible-light irradiation, and (b) the H_2 generation rates of various photocatalysts.

Fig. 7 (a) PL spectra of g-C_3N_4, g-C_3N_4/rGO, g-C_3N_4/CdS and g-C_3N_4/CdS/rGO heterojunctions. (b) Time-resolved fluorescence spectra of the g-C_3N_4, g-C_3N_4/rGO, g-C_3N_4/CdS and g-C_3N_4/CdS/rGO (CCG-10) heterojunctions.

Fig. 8 Photocurrent response of the g-C_3N_4, g-C_3N_4/rGO, g-C_3N_4/CdS and g-C_3N_4/CdS/rGO (CCG-10) heterojunctions.

Fig. 9 Schematic illustration of the charge separation and transformation in g-C_3N_4/CdS/rGO dual-interface nano-composite system under visible-light irradiation.

Fig. 10 Reusability of the CCG-10 photocatalyst for the photocatalytic H_2 production under visible-light irradiation.

Table 1 Kinetic parameters of the fitting decay parameters of pure g-C_3N_4, g-C_3N_4/CdS, g-C_3N_4/rGO and CCG-10 samples

Sample code	Parameter	Lifetime (ns)	Relative percentage (%)	Average life time τ (ns)	χ^2
CN	τ_1	0.98	61.94	2.59	1.140
	τ_2	5.21	38.06		
CN/CdS	τ_1	1.23	52.32	5.20	1.126
	τ_2	9.57	47.68		
CN/rGO	τ_1	1.49	52.61	4.58	1.230
	τ_2	8.02	47.39		
CCG-10	τ_1	3.89	31.17	10.34	1.189
	τ_2	13.26	68.83		

Scheme 1

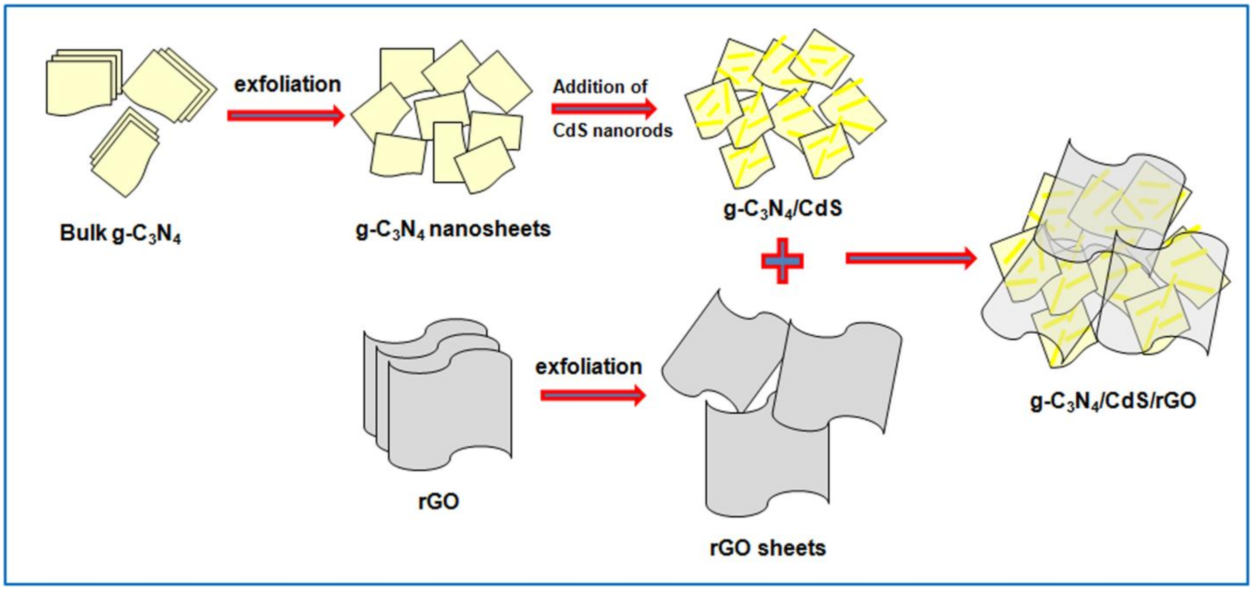

exfoliation
Addition of
CdS nanorods
Bulk g-C_3N_4
g-C_3N_4 nanosheets
g-C_3N_4/CdS
rGO
exfoliation
rGO sheets
g-C_3N_4/CdS/rGO

Fig. 1

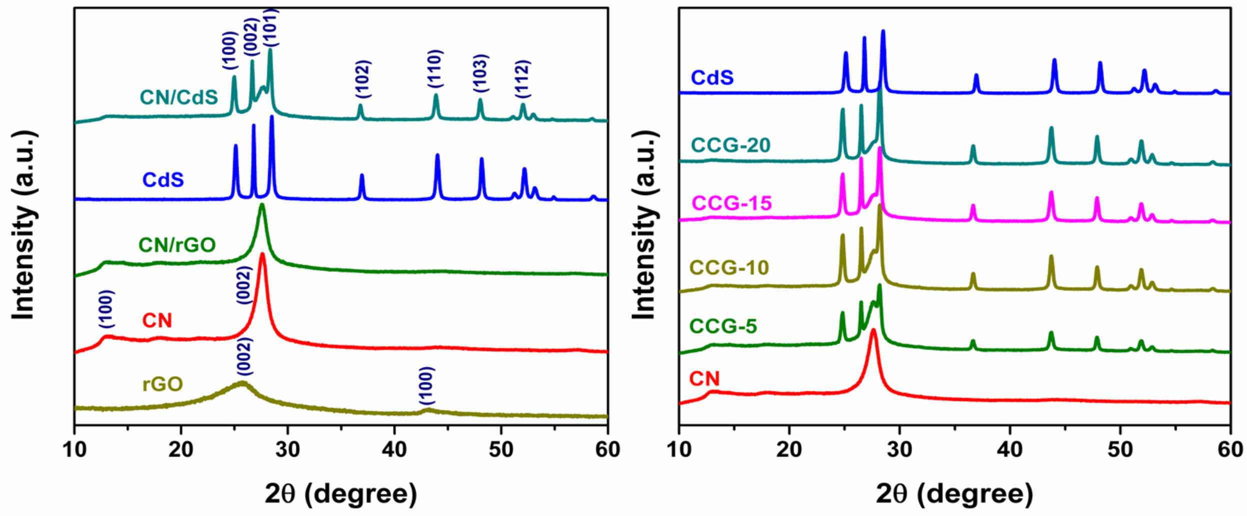
CN/CdS
(100)
(002)
(101)
(102)
(110)
(103)
(112)
CdS
CN/rGO
CN
(100)
(002)
rGO
(002)
(100)
Intensity (a.u.)
2θ (degree)
10
20
30
40
50
60
CdS
CCG-20
CCG-15
CCG-10
CCG-5
CN
Intensity (a.u.)
2θ (degree)
10
20
30
40
50
60

Fig. 2

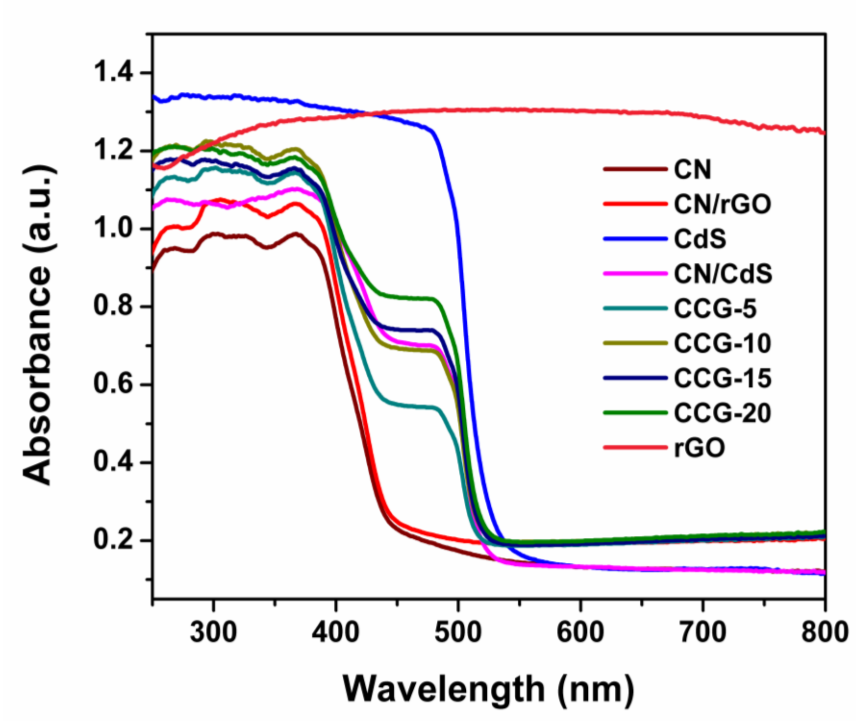
1.4
1.2
1.0
0.8
0.6
0.4
0.2
Absorbance (a.u.)
300
400
500
600
700
800
Wavelength (nm)
CN
CN/rGO
CdS
CN/CdS
CCG-5
CCG-10
CCG-15
CCG-20
rGO

Fig. 3

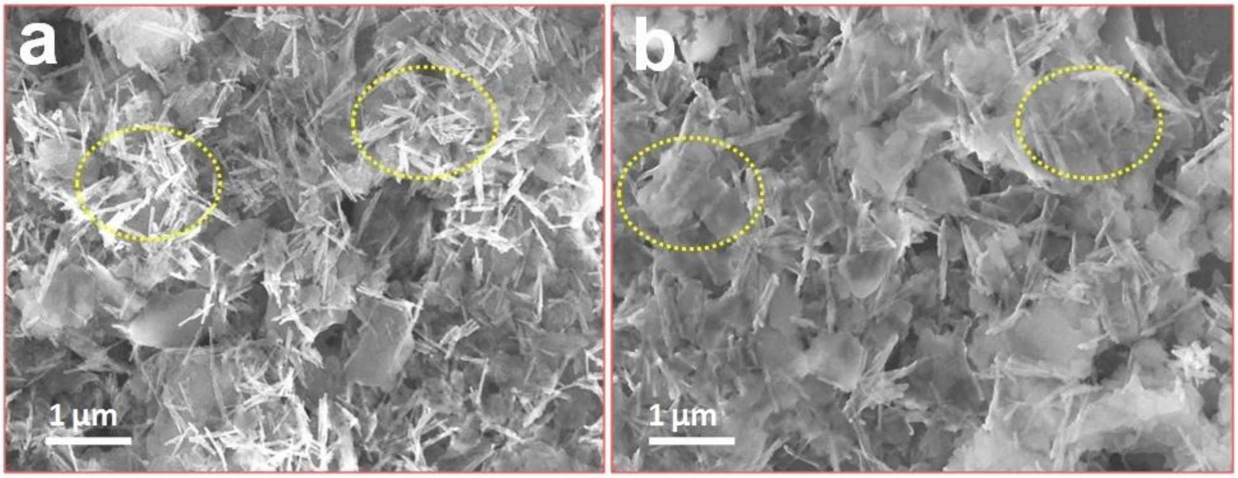

Fig. 4

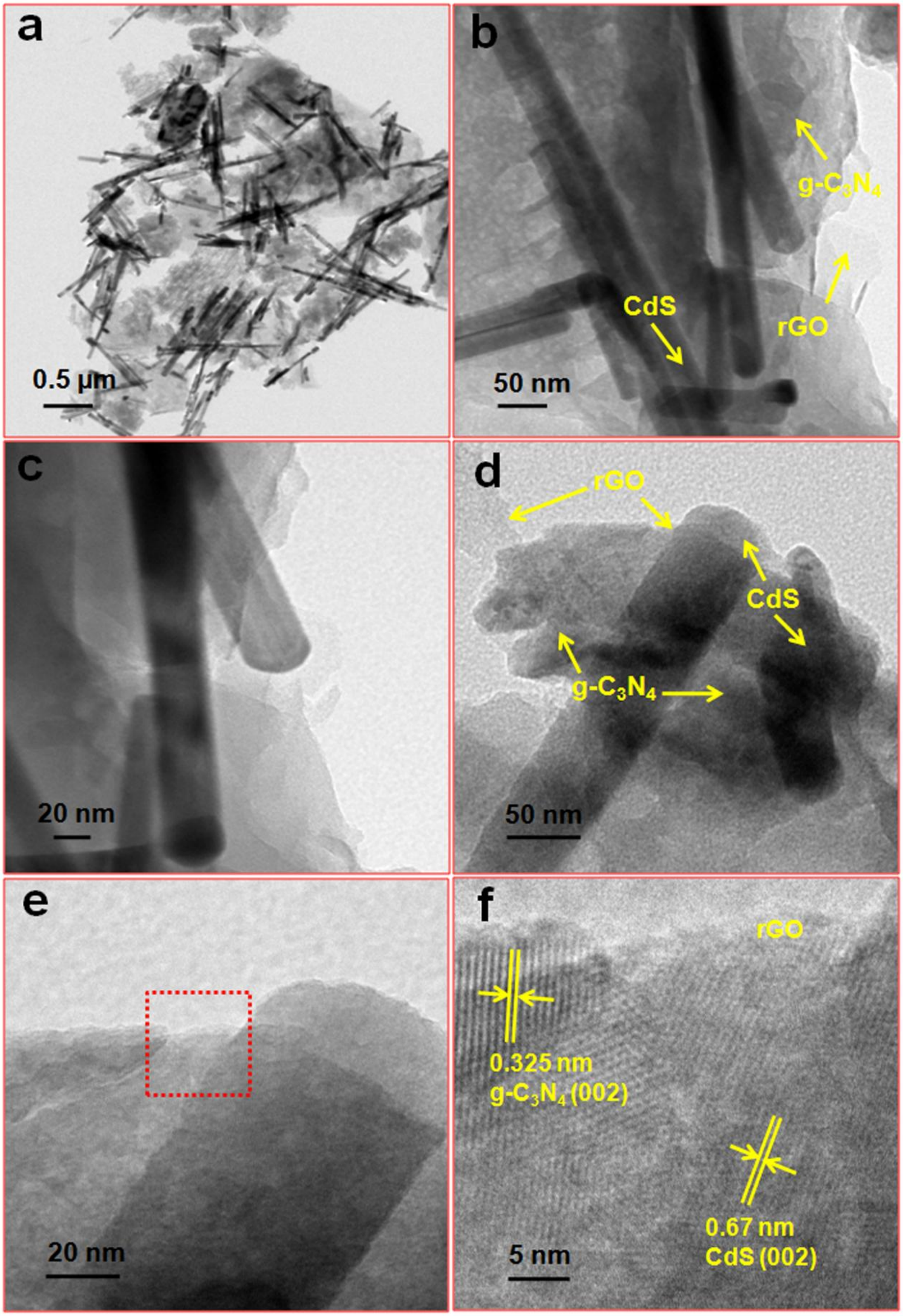

a
0.5 μm
b
g-C3N4
CdS
rGO
50 nm
c
20 nm
d
rGO
CdS
g-C3N4
50 nm
e
20 nm
f
rGO
0.325 nm
g-C3N4 (002)
0.67 nm
CdS (002)
5 nm

Fig. 5

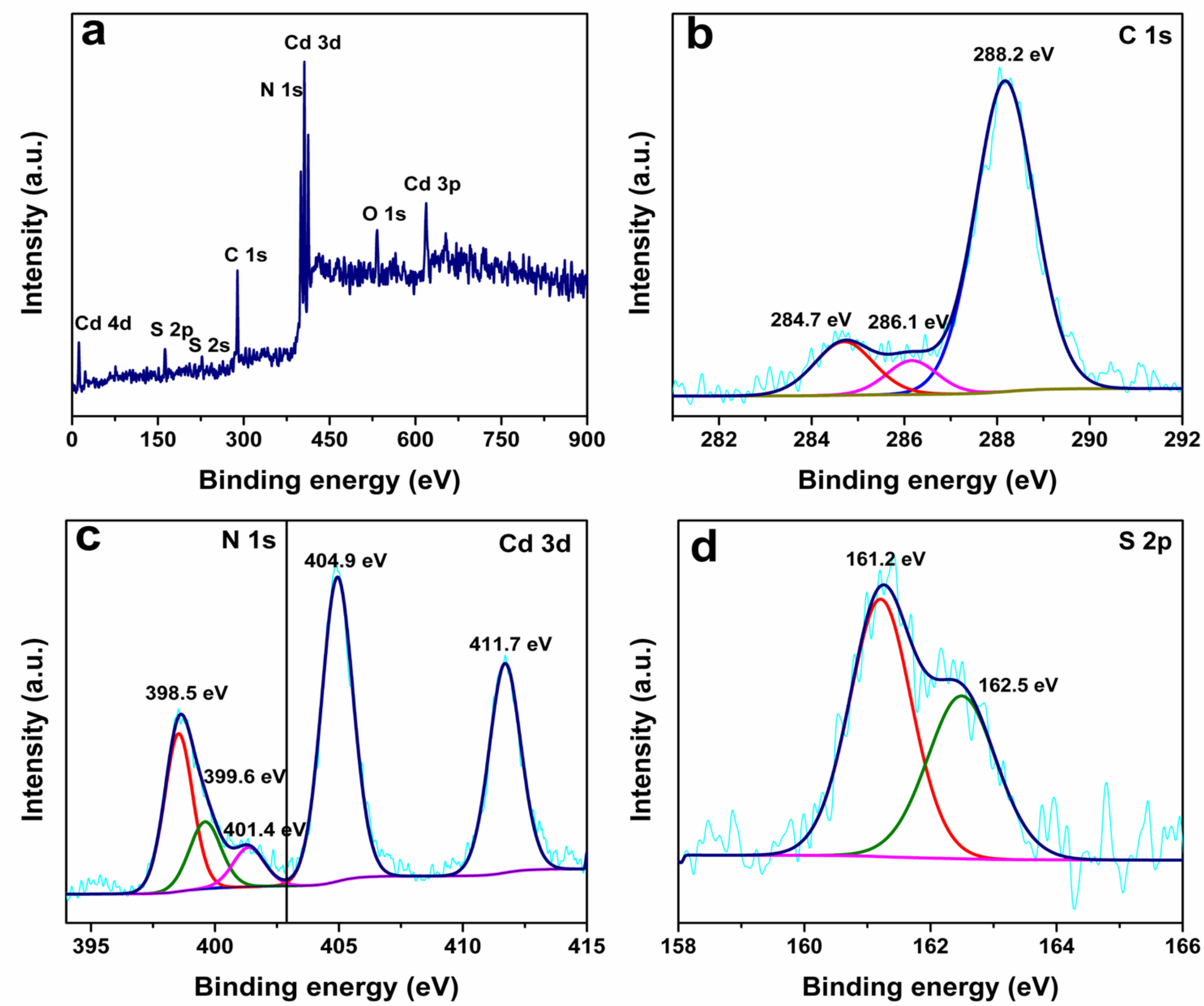
a
Cd 3d
N 1s
Cd 3p
O 1s
C 1s
Cd 4d
S 2p
S 2s
Intensity (a.u.)
Binding energy (eV)
0
150
300
450
600
750
900
b
C 1s
288.2 eV
284.7 eV
286.1 eV
Intensity (a.u.)
Binding energy (eV)
282
284
286
288
290
292
c
N 1s
Cd 3d
404.9 eV
411.7 eV
398.5 eV
399.6 eV
401.4 eV
Intensity (a.u.)
Binding energy (eV)
395
400
405
410
415
d
S 2p
161.2 eV
162.5 eV
Intensity (a.u.)
Binding energy (eV)
158
160
162
164
166

Fig. 6

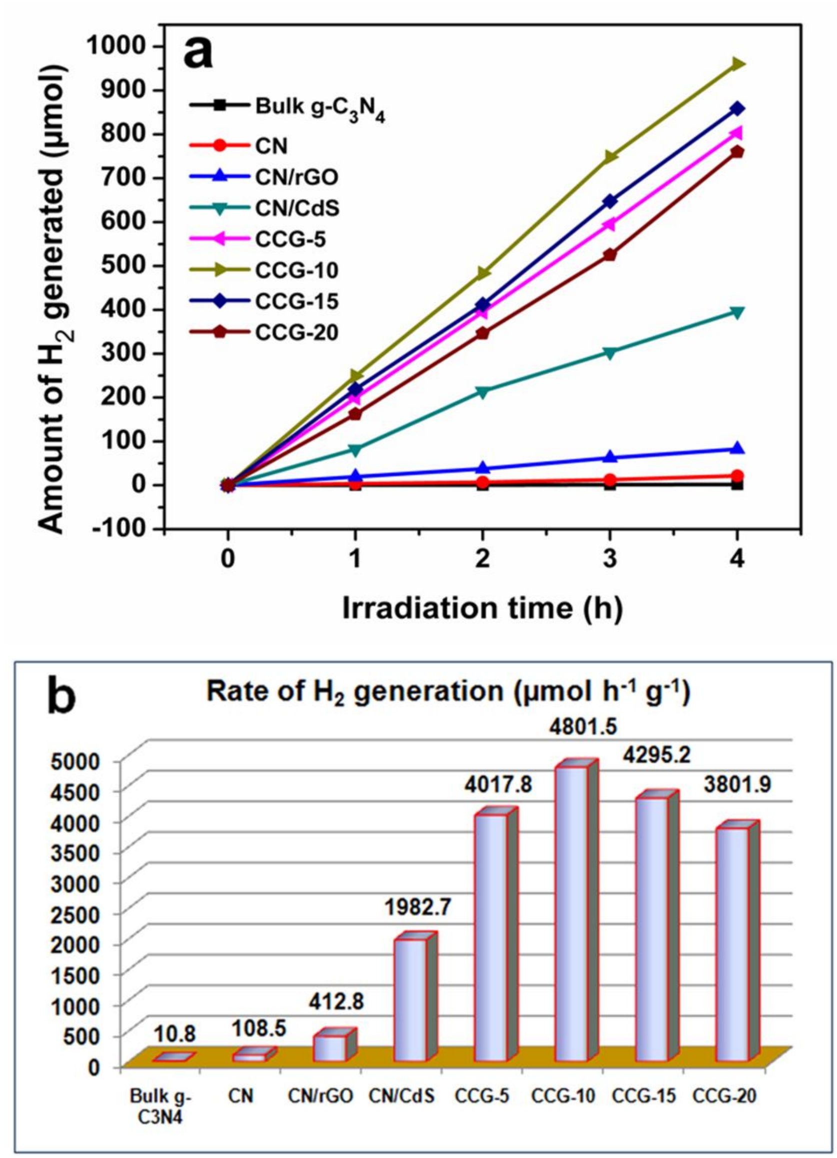

a
Amount of H2 generated (μmol)
Irradiation time (h)
Bulk g-C3N4
CN
CN/rGO
CN/CdS
CCG-5
CCG-10
CCG-15
CCG-20
b
Rate of H2 generation (μmol h-1 g-1)
10.8
108.5
412.8
1982.7
4017.8
4801.5
4295.2
3801.9
Bulk g-C3N4
CN
CN/rGO
CN/CdS
CCG-5
CCG-10
CCG-15
CCG-20

Fig. 7

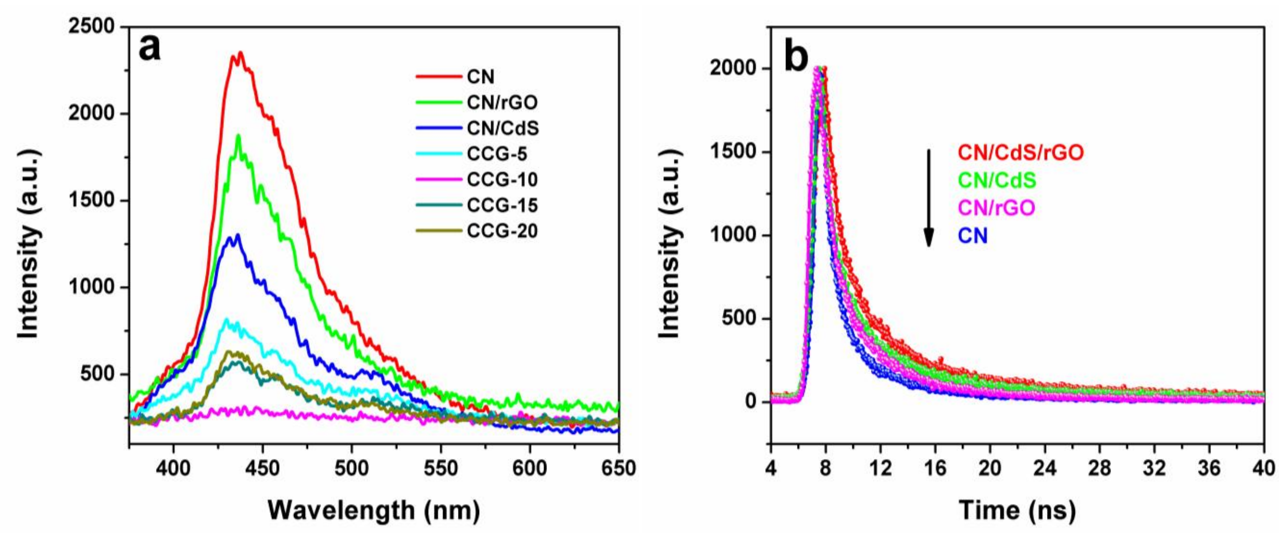
a
CN
CN/rGO
CN/CdS
CCG-5
CCG-10
CCG-15
CCG-20
Intensity (a.u.)
Wavelength (nm)
2500
2000
1500
1000
500
400
450
500
550
600
650
b
CN/CdS/rGO
CN/CdS
CN/rGO
CN
Intensity (a.u.)
Time (ns)
2000
1500
1000
500
0
4
8
12
16
20
24
28
32
36
40

Fig. 8

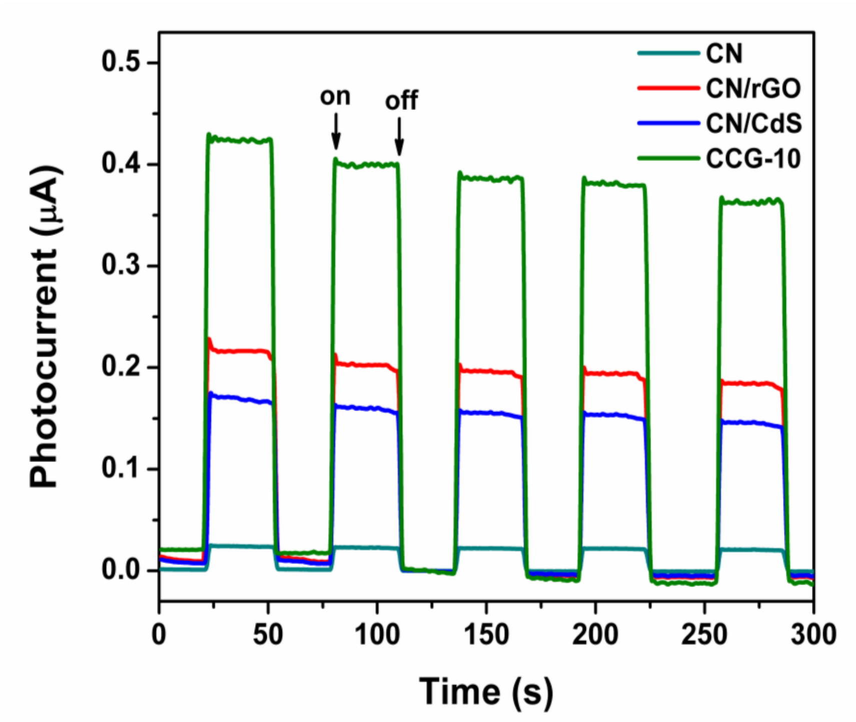

CN
CN/rGO
CN/CdS
CCG-10
on
off
Photocurrent (μA)
0.5
0.4
0.3
0.2
0.1
0.0
0
50
100
150
200
250
300
Time (s)

Fig. 9

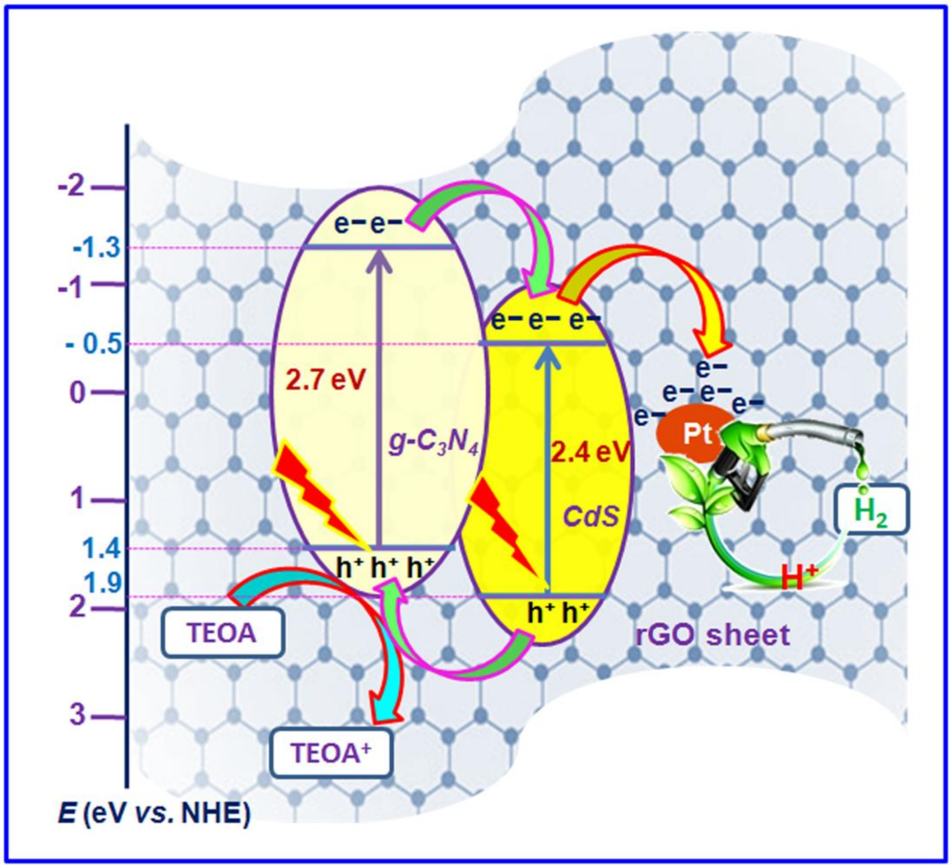
-2
-1.3
-1
- 0.5
0
1
1.4
1.9
2
3
E (eV vs. NHE)
e− e−
2.7 eV
g-C3N4
h+ h+ h+
e− e− e−
2.4 eV
CdS
h+ h+
TEOA
TEOA+
e−
e− e− e−
e− e−
Pt
H2
H+
rGO sheet

Fig. 10

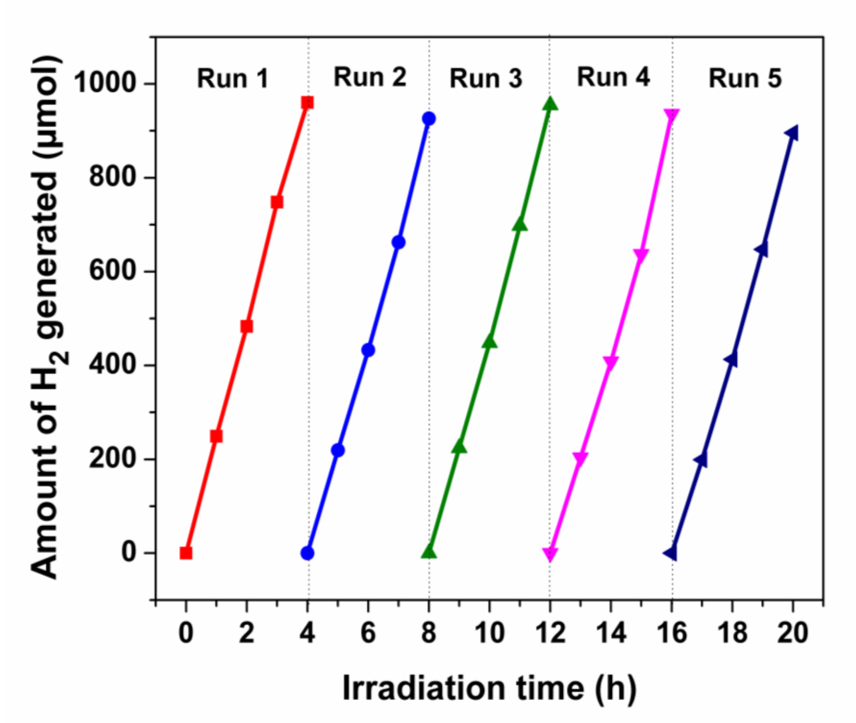

Run 1
Run 2
Run 3
Run 4
Run 5
Amount of H_2 generated (μmol)
0
200
400
600
800
1000
0
2
4
6
8
10
12
14
16
18
20
Irradiation time (h)